ChemPubSoc Europe

DOI: 10.1002/cctc.201300565

XAFS Study on the Specific Deoxidation Behavior of Iron Titanate Catalyst for the Selective Catalytic Reduction of NO_x with NH_3

Fudong Liu, Hong He,* and Lijuan Xie[a]

The environmentally friendly catalyst iron titanate ($FeTiO_x$) was reported to be very active for the selective catalytic reduction of NO_x with NH_3 (NH_3-SCR), with high N_2 selectivity and H_2O/SO_2 durability in the medium temperature range, and the specific microstructure of iron titanate crystallites as the active phase was determined. In consideration of the probable existence of a redox cycle between Fe^{3+} and Fe^{2+} species in the NH_3-SCR reaction, the deoxidation behavior of the $FeTiO_x$ catalyst in an H_2 temperature-programmed reduction process was studied extensively by X-ray absorption near-edge structure (XANES) and extended X-ray absorption fine-structure (EXAFS) methods. Owing to the presence of an electronic inductive effect between Fe and Ti species in the unique edge-shared Fe^{3+}–$(O)_2$–Ti^{4+} structure, the reducibility of Fe^{3+} species in the $FeTiO_x$ catalyst was greatly enhanced compared with that in pristine Fe_2O_3, leading to the higher oxidation ability of Fe species in $FeTiO_x$. In the H_2 temperature-programmed reduction process, the well-dispersed Fe^{3+} species in iron titanate crystallites could be totally converted into Fe^{2+} in the form of ilmenite $FeTiO_3$ below 500 °C, whereas pristine Fe_2O_3 could only be reduced to Fe_3O_4 up to this temperature point. The typical NH_3-SCR reaction is usually conducted below 500 °C, and the enhanced oxidation ability of Fe^{3+} species in $FeTiO_x$ catalyst is responsible for its excellent catalytic NO_x reduction performance at low temperatures. Based on XANES linear fitting and EXAFS curve-fitting results, the specific deoxidation process of the $FeTiO_x$ catalyst was proposed, which can provide useful information for the characterization of the microstructure and redox ability of active sites simultaneously in mixed oxide catalysts for certain catalytic reactions.

Introduction

The greatly increased demand for the use of fossil fuels including coal and oil nowadays has led to the significant growth in emission of air pollutants including particulate matter, sulfur dioxide, and nitrogen oxides (NO_x), especially in the developing countries with rapid increase in gross domestic product. Owing to the widely used dust-removal equipment and desulfurizing units, the particulate matter and SO_2 can be effectively controlled to a certain extent, whereas the ultrafine particles and NO_x become the key targets for air-pollutant control in the next steps. NO_x, including NO and NO_2 emitted from stationary and mobile sources, are major air pollutants resulting in acid rain, photochemical smog, respiratory disease,[1,2] and possibly even severe haze pollution, and need to be controlled effectively in accordance with more and more stringent regulations worldwide. Selective catalytic reduction of NO_x with NH_3 (NH_3-SCR) under oxygen-rich conditions is one of the most efficient technologies for the catalytic removal of NO_x, and the earliest commercial catalyst system was WO_3- or MoO_3-promoted V_2O_5/TiO_2, with high NH_3-SCR performance and SO_2 durability in the medium or high temperature ranges.[3–6] Although this catalyst system has been utilized for several decades in industry, some disadvantages still exist such as a narrow operation temperature window, low N_2 selectivity and poor stability at high temperatures, and, more importantly, the biological toxicity of the active V_2O_5 phase, restricting its further application especially for the NO_x reduction process for mobile sources such as diesel engines.[3,7,8] Therefore, more and more researchers now devote themselves to the development of new, highly efficient and environmentally friendly NH_3-SCR catalysts with improved low-temperature deNO_x efficiency, hydrothermal stability or resistance to co-existing pollutants, including zeolite catalysts promoted by metal cations (e.g., Fe-ZSM-5, Fe-BEA, Cu-ZSM-5, Cu-beta, Cu-CHA)[9–20] and single metal oxide, supported type, or mixed oxide catalysts (e.g., γ-Fe_2O_3 nanorods, Fe_2O_3/WO_3/ZrO_2, $Ti_{0.9}Fe_{0.1}O_{2-\delta}$, Ce-P-O, $CeTiO_x$, $CeWO_x$, MnO_x, $(Fe_{3-x}Mn_x)_{1-\delta}O_4$).[21–29]

In our previous study, we reported a novel, environmentally benign iron titanate ($FeTiO_x$) catalyst for NH_3-SCR of NO_x prepared by a facile coprecipitation method, achieving high deNO_x efficiency, N_2 selectivity, and H_2O/SO_2 durability in the medium temperature range.[30–32] The NH_3-SCR mechanisms in the low- and high-temperature ranges were proposed according to in situ diffuse reflectance infrared Fourier transform spectroscopy and mass spectrometry to detect the surface-adsorbed species and gaseous components, respectively, in the SCR reaction,[33] most likely involving the redox cycle of $Fe^{3+} \leftrightarrow Fe^{2+}$ for the activation of reactants including NH_3 and NO. Owing to the strong interaction between Fe and Ti species,

[a] Dr. F. Liu, Prof. H. He, L. Xie
Research Center for Eco-Environmental Sciences
Chinese Academy of Sciences
18 Shuangqing Road, Beijing 100085 (P.R. China)
Fax: (+86) 10-62849123
E-mail: honghe@rcees.ac.cn

the active phase in this $FeTiO_x$ catalyst was mainly in the form of crystallites, the structure of which was rather difficult to characterize by conventional XRD, Raman spectra, or TEM, which usually require long-range order in the target materials. Therefore, the X-ray absorption fine structure (XAFS) method was used for the systematic structural characterization of this $FeTiO_x$ catalyst,[34] which is very sensitive to the electronic state and local structure of specific central atoms. For the vanadium-free catalyst systems in the reported works mentioned above, the catalytic $deNO_x$ performance has usually been investigated in detail, yet the comprehensive investigation of their structure–activity relationships in the NH_3-SCR reaction is still largely lacking. In particular, many researchers have only paid attention to the microstructure of the active phase in NH_3-SCR catalysts and ignored the redox ability of the active species, which is actually not beneficial for the understanding of reaction mechanisms. Herein, the specific deoxidation behavior of Fe species in the $FeTiO_x$ catalyst was sequentially investigated by using the XAFS method in combination with H_2 temperature programmed reduction (H_2-TPR) experiments, which can provide useful information about the redox ability of Fe species having a special microstructure, to better understand the intrinsic reason for its high catalytic $deNO_x$ efficiency in the NH_3-SCR reaction.

Results and Discussion

NH_3-SCR performance of the $FeTiO_x$ catalyst and its microstructure

The NH_3-SCR performance of the $FeTiO_x$ catalyst compared with that of anatase TiO_2 and hematite Fe_2O_3 is shown in Figure 1. As we can clearly see, the $FeTiO_x$ catalyst exhibited high NH_3-SCR performance over a broad temperature range, with over 80% NO_x conversion obtained from 200 to 400 °C. The pristine TiO_2 prepared under our conditions exhibited no $deNO_x$ efficiency below 350 °C, and only 30% NO_x conversion could be achieved at temperatures as high as 400 °C. As for pristine Fe_2O_3 also prepared by ourselves, the maximum NO_x conversion could only reach 60%, and the operation temperature window was rather narrow. These results indicate that the coexistence of Fe and Ti species in the $FeTiO_x$ catalyst is important to obtain high $deNO_x$ efficiency, which can be attributed to the strong interaction between Fe and Ti species leading to larger surface areas, smaller particle sizes, higher NO oxidation ability and more abundant surface acid sites.[31,32]

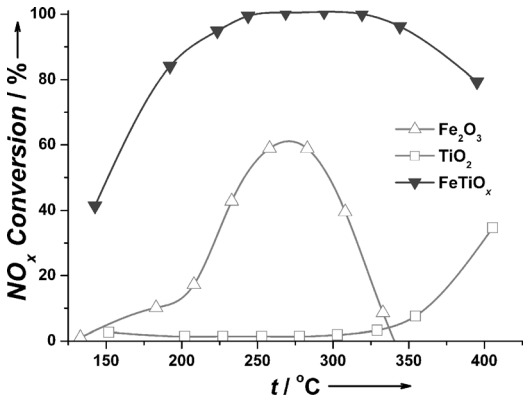

Figure 1. NO_x conversions as a function of temperature in the NH_3-SCR reaction over $FeTiO_x$ catalyst and references hematite Fe_2O_3 and anatase TiO_2, respectively. Reaction conditions: $[NO]=[NH_3]=500$ ppm, $[O_2]=5$ vol%, 0.6 mL catalyst, and total flow rate of 500 mL min^{-1} yielding a gas hourly space velocity of 50000 h^{-1}.

As shown by the high-resolution TEM (HRTEM) images in Figure 2A and B,[32] both the anatase TiO_2 (103.5 m^{2}g^{-1}) and hematite Fe_2O_3 (42.5 m^{2}g^{-1}) were well crystallized with relatively large particle sizes, lacking rich surface defects for the adsorption and activation of reactants in the NH_3-SCR reaction. Possibly owing to the very similar ion radii of Fe^{3+} (0.645 Å) and Ti^{4+} (0.605 Å),[35] in the $FeTiO_x$ catalyst the Fe species and Ti species could interdiffuse in a homogeneous state resulting in the formation of iron titanate crystallites with small particle size and relatively large surface area (245.3 m^{2}g^{-1}), which could supply more surface defects and active sites for the occurrence of the NH_3-SCR reaction. As indicated by the HRTEM image of the $FeTiO_x$ catalyst (Figure 2C), no discernible lattice fringes could be observed, which was in good accordance with the broad diffraction bumps in XRD patterns and indistinct scattering bands in Raman spectra as presented in our previ-

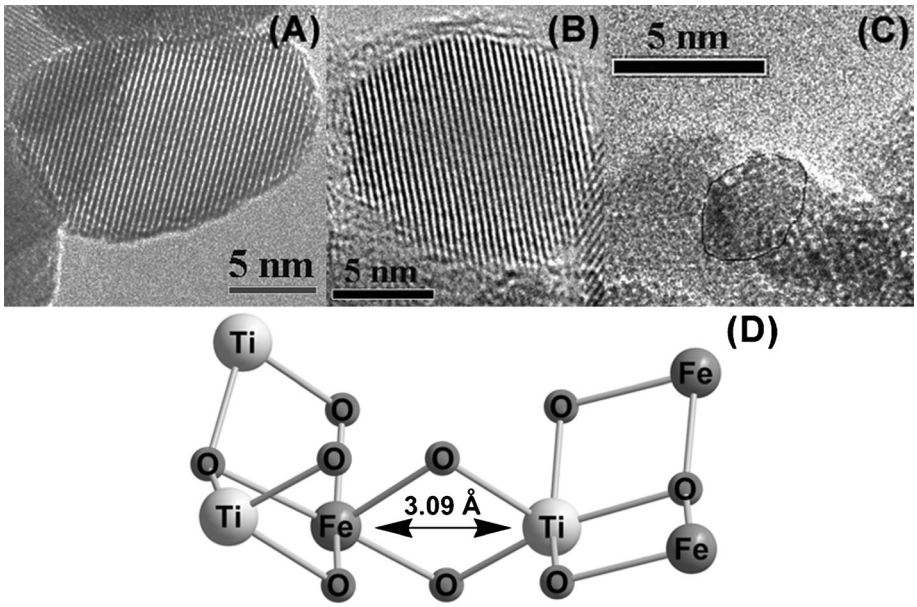

Figure 2. HRTEM images of A) hematite Fe_2O_3, B) anatase TiO_2, and C) $FeTiO_x$ catalyst,[32] and D) proposed structural model of $FeTiO_x$ catalyst derived from EXAFS curve-fitting results[34].

ous study.[31] Therefore, the XAFS method, which is very suitable to be used for the characterization of such amorphous or microcrystalline materials with no long-range order, was used to elucidate the microstructure of iron titanate crystallite in $FeTiO_x$ catalyst in detail. Using X-ray absorption near-edge structure (XANES) and extended X-ray absorption fine structure (EXAFS) data in combination with DFT calculations to simulate the electronic density, we concluded that, different from the crystal structure of Fe^{3+} species in hematite Fe_2O_3 and Fe_2O_3/TiO_2 supported-type catalyst, a homogeneous Fe^{3+}–$(O)_2$–Ti^{4+} structure was clearly formed in the $FeTiO_x$ catalyst, in which the Fe^{3+} species and Ti^{4+} species were strongly linked in an edge-shared fashion (as shown by the structural model in Figure 2 D).[34] The electronic inductive effect was confirmed to be present between Fe^{3+} species and Ti^{4+} species by XANES and X-ray photoelectron spectroscopy (XPS) results,[31,32,34] effectively reducing the electron density around Fe^{3+} species thus leading to the enhancement of NO adsorption, oxidation ability and finally the low temperature NH_3-SCR performance. Furthermore, the Fe^{3+}–$(O)_2$–Ti^{4+} structure also showed high durability to SO_2 poisoning in the NH_3-SCR reaction mainly attributable to the close and homogeneous combination of Fe species and Ti species as well as the easy decomposition of sulfate on Ti sites.[36] In previous studies by other researchers, the importance of the complex generated between the active phase and catalyst support was also emphasized, such as the Ag–O–Al species in Ag/Al_2O_3 catalysts for the CH_4-SCR of NO_x[37] and the Ce–O–Ti species in $CeTiO_x$ catalysts for the NH_3-SCR of NO_x.[38] Therefore, the study on the microstructure and chemical properties of such catalytically active species is an important and universal issue in the field of heterogeneous catalysis.

H_2-TPR results of $FeTiO_x$ catalyst and reference samples

Although the microstructure of iron titanate crystallites in the $FeTiO_x$ catalyst has been clearly elucidated in our previous study, the reducibility of the Fe species has not been well recognized although it is actually very important for the completion of the redox cycle in the NH_3-SCR reaction. Therefore, an H_2-TPR experiment for the $FeTiO_x$ catalyst was performed, using hematite Fe_2O_3, anatase TiO_2, and ilmenite $FeTiO_3$ as references, and the results are shown in Figure 3.

As we can clearly see, no notable reduction peaks were present for pristine TiO_2, which indicates that the anatase support did not participate in the redox cycle for the NH_3-SCR reaction, owing to its lack of reducibility, only supplying adsorption sites for the reactants in the deNO_x process. As for pristine Fe_2O_3, there were two H_2 consumption peaks located at 405 and 725 °C, respectively. According to the baseline of the H_2 signal, the Fe species in hematite Fe_2O_3 started to be reduced at approximately 200 °C, similar to the initial reduction process of γ-Fe_2O_3 nanorods prepared by Mou et al..[27] Possibly owing to the relatively large particle sizes and difficult H_2 diffusion, the first reduction peak at 405 °C did not exhibit Gaussian symmetry, and the second reduction peak at 725 °C, overlapping with a shoulder reduction peak above 800 °C, did not return to the baseline until as high as 900 °C, which was different to a certain

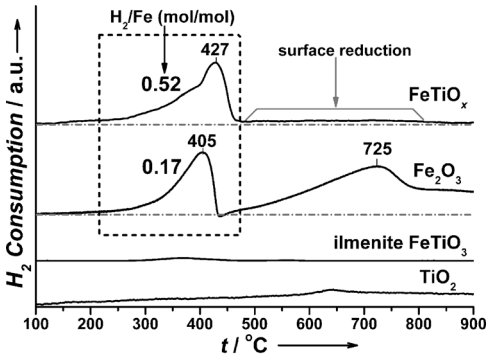

Figure 3. H_2-TPR profiles of $FeTiO_x$ catalyst, hematite Fe_2O_3, anatase TiO_2,[31] and ilmenite $FeTiO_3$.

extent from the reduction processes observed for γ-Fe_2O_3 nanorods enclosed by abundant reactive {1 1 0} and {1 0 0} crystal facets.[27] However, we could still calculate the H_2/Fe molar ratio for the reduction peak at low temperature to confirm the reduction process of Fe species in hematite Fe_2O_3 below 500 °C, which is typically the maximum reaction temperature for the NH_3-SCR reaction. As shown in Figure 3, the H_2/Fe molar ratio for the reduction peak of Fe_2O_3 at 405 °C was calculated to be 0.17, which was exactly consistent with the reduction process from Fe_2O_3 to Fe_3O_4. Further raising the reduction temperature could lead to the formation of FeO or metallic Fe^0, yet different reduction mechanisms have been proposed by former researchers including the two-stage reduction of $3\,Fe_2O_3 \rightarrow 2\,Fe_3O_4 \rightarrow 6\,Fe$[39,40] and the three-stage reduction of $3\,Fe_2O_3 \rightarrow 2\,Fe_3O_4 \rightarrow 6\,FeO \rightarrow 6\,Fe$.[27,41,42] XANES measurements could clearly discriminate the possible mixed Fe species in reduced Fe_2O_3, which will be discussed in detail below.

Based on the H_2-TPR results of TiO_2 and Fe_2O_3, the H_2 reduction peaks observed for the $FeTiO_x$ catalyst could be only ascribed to the reduction of Fe species, because the Ti species were barely reduced under these conditions. In the $FeTiO_x$ catalyst with much higher NH_3-SCR performance than TiO_2 and Fe_2O_3, the Fe species started to be reduced at approximately 150 °C, 50 °C lower than pristine Fe_2O_3. This result clearly shows that the oxygen species (mainly surface-adsorbed oxygen reduced at low temperatures) in the $FeTiO_x$ catalyst is more labile probably owing to the strong interaction between Fe species and Ti species, leading to rich surface defects for the activation of oxygen. Interestingly, totally different from the reduction processes of Fe_2O_3, only one composite reduction peak was observed for the $FeTiO_x$ catalyst with the maximum H_2 consumption rate at 427 °C. According to the calculated H_2/Fe molar ratio of 0.52, the Fe^{3+} species in the $FeTiO_x$ catalyst could be totally reduced to Fe^{2+} species below 500 °C, probably resulting in the transformation of iron titanate crystallite $Fe^{3+}TiO_x$ to ilmenite $Fe^{2+}TiO_3$. Although the temperature point for the maximum H_2 consumption rate of the $FeTiO_x$ catalyst (427 °C) was higher than that of hematite Fe_2O_3 (405 °C), the reducibility of Fe species in the former catalyst was actually much higher than that in the latter sample. Therefore, the synergistic combination of Fe species and Ti species in the $FeTiO_x$ catalyst not only produced a unique edge-shared Fe^{3+}–$(O)_2$–

Ti^{4+} structure, but also resulted in the easier deoxidation behavior of Fe species at low temperatures, which is beneficial to the completion of the redox cycle for the NH_3-SCR reaction and thus the improvement of low-temperature $deNO_x$ efficiency. A similar phenomenon has also been reported by Li et al.,[38] in which the Ce species in the form of Ce–O–Ti linkages in a $CeTiO_x$ catalyst with excellent SCR performance showed higher reducibility than that in pristine CeO_2. Above 500 °C, the H_2 reduction curve of the $FeTiO_x$ catalyst was slightly above the baseline, which could be attributed to the reduction of surface layers of $Fe^{2+}TiO_3$ to metallic Fe^0 and leaving TiO_2 (probably in the rutile phase after 900 °C reduction). The in situ formed surface metallic Fe^0 might form clusters or particles on the $Fe^{2+}TiO_3$ phase mainly caused by the relatively weak interaction between metal and oxide support. At the same time, no further reduction of Fe^{2+} species in $Fe^{2+}TiO_3$ phase was observed even at temperatures as high as 900 °C. A similar phenomenon was also found on the ilmenite $FeTiO_3$ reference, for which the H_2-TPR profile revealed no obvious reduction peak of Fe^{2+} species in the whole temperature range. This is another interesting characteristic of the H_2 reduction behavior of the $FeTiO_x$ catalyst, and the abovementioned points of view are verified by the following XANES linear-fitting results and EXAFS curve-fitting results.

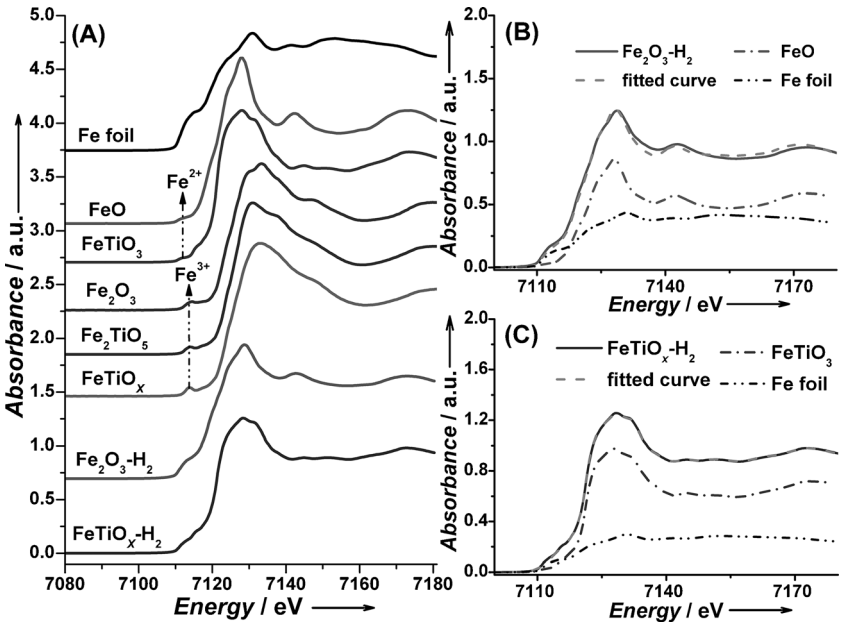

Figure 4. A) Normalized XANES spectra of Fe K edge in Fe-containing samples; B) XANES linear-fitting results of Fe K edge in hematite Fe_2O_3 after H_2 reduction using FeO and Fe as references; C) XANES linear-fitting results of Fe K edge in $FeTiO_x$ catalyst after H_2 reduction using $FeTiO_3$ and Fe as references. Samples specified by "–H_2" refer to samples after the H_2-TPR procedure to 900 °C; see Experimental Section.

XANES results of Fe K, Ti K edges

Using Fe foil, FeO, $FeTiO_3$, Fe_2O_3, and Fe_2TiO_5 as references, the XANES spectra of the Fe K edge in $FeTiO_x$ catalysts before and after H_2 reduction together with H_2-reduced Fe_2O_3 were recorded, as shown in Figure 4A. According to the pre-edge peak position, the Fe species in the $FeTiO_x$ catalyst was mainly present in the form of Fe^{3+}, similar to those in Fe_2O_3 and Fe_2TiO_5. According to the first-order derivatives of Fe K XANES as reported in our previous study,[34] the absorption edge energy of Fe^{3+} species in the $FeTiO_x$ catalyst (7123.6 eV) was higher than those in Fe_2O_3 (7123.2 eV) and Fe_2TiO_5 (7123.4 eV), mainly owing to the presence of the most abundant Fe^{3+}–$(O)_2$–Ti^{4+} structure with an electronic inductive effect between Fe^{3+} and Ti^{4+} species, resulting in the higher oxidation ability of Fe^{3+} species. This result confirmed by XPS data in our previous study[31] is also in good accordance with the H_2-TPR results, in which the Fe^{3+} species in the $FeTiO_x$ catalyst is much more easily reduced than that in pristine Fe_2O_3. Besides, the highest pre-edge peak intensity and the smoothest post-edge region of Fe K XANES in the $FeTiO_x$ catalyst indicate that the Fe^{3+} species in this catalyst exhibits the most severe structure distortion and the smallest particle size, which is beneficial to the generation of rich surface defects and thus high catalytic performance. The similarity of Fe K XANES patterns between the $FeTiO_x$ catalyst and the Fe_2TiO_5 reference indicates that the iron titanate crystallites may have some Fe–O or Fe–O–Ti coordination shells similar to those in Fe_2TiO_5, which can be verified by EXAFS results. As for the H_2-reduced Fe_2O_3 and $FeTiO_x$ samples, both XANES patterns of the Fe K edge showed marked changes, with the shift of absorption edges towards the lower energy range and the substitution of the former pre-edge peaks by new pre-edge peaks characteristic of metallic Fe^0, mixing with other pre-edge peak features. The post-edge regions of Fe K XANES in H_2-reduced Fe_2O_3 and $FeTiO_x$ samples also exhibited mixed patterns, not similar to those of either FeO or $FeTiO_3$ individually. Therefore, Fe K XANES linear fitting was performed for Fe_2O_3 and $FeTiO_x$ samples after H_2 reduction by using FeO, $FeTiO_3$ and Fe foil as references to better confirm the existing state of Fe species in these H_2-reduced samples, and the fitting results are shown in Figure 4B and 4C, respectively. By linear combination of Fe K XANES data in FeO and Fe foil, the XANES spectrum of H_2-reduced Fe_2O_3 is well simulated with high fitting degree. As the fitting data in Table 1 reveal, the contribution of FeO and metallic Fe to the overall Fe K XANES of H_2-reduced Fe_2O_3 is approximately 66.3% and 33.7%, respectively. This result suggests that after the reduction of Fe_2O_3 to Fe_3O_4 below 500 °C, the Fe species could be reduced further to FeO and then to metallic Fe^0 mainly following a three-stage reduction mechanism as mentioned above.[27,41,42] As for the H_2-reduced $FeTiO_x$ catalyst, no FeO phase can be abstracted from the Fe K XANES spectrum, con-

Table 1. XANES linear-fitting results of Fe K edge and Ti K edge in hematite Fe_2O_3 and $FeTiO_x$ catalyst after H_2 reduction.

Sample	Fe K XANES		Ti K XANES	
	Ref.	Molar ratio [%]	Ref.	Molar ratio [%]
Fe_2O_3-H_2	FeO	66.3	–	–
	Fe foil	33.7	–	–
$FeTiO_x$-H_2	$FeTiO_3$	76.6	$FeTiO_3$	72.5
	Fe foil	23.4	rutile TiO_2	27.5

firming again that no Fe_2O_3 phase existed in the as-prepared $FeTiO_x$ catalyst and a new structure of Fe species was indeed formed. Using $FeTiO_3$ and Fe foil as references, the Fe K XANES of the $FeTiO_x$ catalyst after H_2 reduction is well simulated with high fitting degree, which is consistent with our viewpoint concerning the H_2-TPR result in Figure 3. As shown in Table 1, the contribution of $FeTiO_3$ and metallic Fe to the overall Fe K XANES of the $FeTiO_x$ catalyst after H_2 reduction is approximately 76.6% and 23.4%, respectively. Owing to the homogeneous state of the Fe^{3+}–$(O)_2$–Ti^{4+} structure in the iron titanate crystallites, the $FeTiO_x$ catalyst could be uniformly transformed into $FeTiO_3$ at relatively low temperatures, revealing a deoxidation behavior totally different from that of pristine Fe_2O_3. Further increasing the reduction temperature indeed only led to the formation of metallic Fe^0 cluster or particles, leaving a majority of Fe species in the form of ilmenite $FeTiO_3$. Owing to the stoichiometric balance between Fe and Ti species (1:1) in the as-prepared $FeTiO_x$ catalyst, the formation of metallic Fe^0 in the H_2-reduced sample must result in the formation of excess TiO_2 phase, which can be verified by the following Ti K XANES results.

The XANES spectra of Ti K edge in $FeTiO_x$ catalysts before and after H_2 reduction were recorded by using Ti foil, anatase TiO_2, rutile TiO_2, $FeTiO_3$, and Fe_2TiO_5 as references, and the results are shown in Figure 5 A. As we can clearly see, not only the pre-edge peak shape but also the post-edge region of Ti K XANES in the as-prepared $FeTiO_x$ catalyst was totally different from those in anatase TiO_2 and rutile TiO_2, indicating the presence of Ti^{4+} species in another coordination state. Notably, the XANES pattern of the Ti K edge in $FeTiO_x$ catalyst was similar to that in Fe_2TiO_5 but with higher pre-edge peak intensity and smoother post-edge region, suggesting that the iron titanate crystallites with smaller particle sizes have Ti–O or Ti–O–Fe coordination shells similar to those in Fe_2TiO_5 yet with more severe structure distortion, similar to the conclusions from the Fe K XANES experiments. Based on the first-order derivatives of Ti K XANES in our previous study,[34] the absorption edge energy of Ti^{4+} species in the $FeTiO_x$ catalyst (4983.4 eV) was lower than those in anatase TiO_2 (4985.5 eV) and Fe_2TiO_5 (4984.3 eV), which can be simply explained by the reverse electronic inductive effect between Fe^{3+} and Ti^{4+} species in the most abundant Fe^{3+}–$(O)_2$–Ti^{4+} structures. As for the H_2-reduced $FeTiO_x$ catalyst, both the pre-edge peak and post-edge region revealed a marked change, exhibiting a mixed state of Ti^{4+} species. As presented in Figure 5 B, the XANES spectrum of the Ti K edge in the $FeTiO_x$ catalyst after H_2 reduction can be well simulated by using ilmenite $FeTiO_3$ and rutile TiO_2 as references, which is in good accordance with the H_2-TPR and Fe K XANES results. The contributions of ilmenite $FeTiO_3$ and rutile TiO_2 to the overall XANES result from the perspective of Ti K edge are approximately 72.5% and 27.5%, respectively (Table 1), confirming again that the formation of metallic Fe^0 resulted in the presence of residual rutile TiO_2 in an approximately equivalent amount. In brief, not only from the Fe K XANES results but also from the Ti K XANES results, we can conclude that the Fe^{3+} and Ti^{4+} species are homogeneously dispersed at the atomic scale, and the electronic inductive effect between them results in the enhancement of oxidation ability of Fe species leading to the more facile deoxidation behavior of the $FeTiO_x$ catalyst, which is beneficial to the completion of the redox cycle in the NH_3-SCR reaction and thus the promotion of $deNO_x$ efficiency.

EXAFS results of Fe K and Ti K edges

To further confirm the existing states of Fe species in the $FeTiO_x$ catalyst and Fe_2O_3 sample after H_2 reduction, the EXAFS data of the Fe K edge were curve-fitted by using the least-square method. In Figure 6 A, the Fourier transforms of filtered

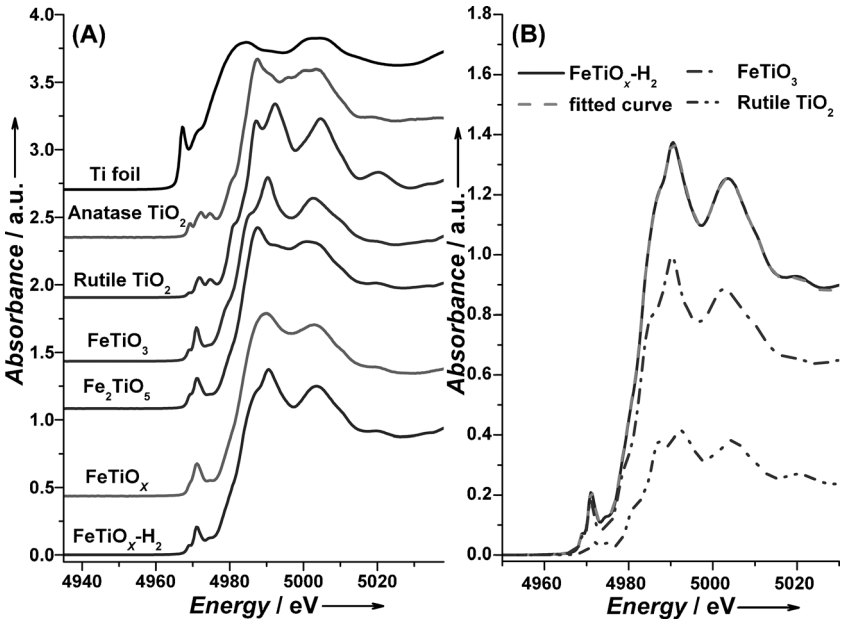

Figure 5. A) Normalized XANES spectra of Ti K edge in Ti-containing samples; B) XANES linear fitting results of Ti K edge in $FeTiO_x$ catalyst after H_2 reduction using $FeTiO_3$ and Fe as references. Samples specified by "–H_2" refer to samples after the H_2-TPR procedure to 900 °C; see Experimental Section.

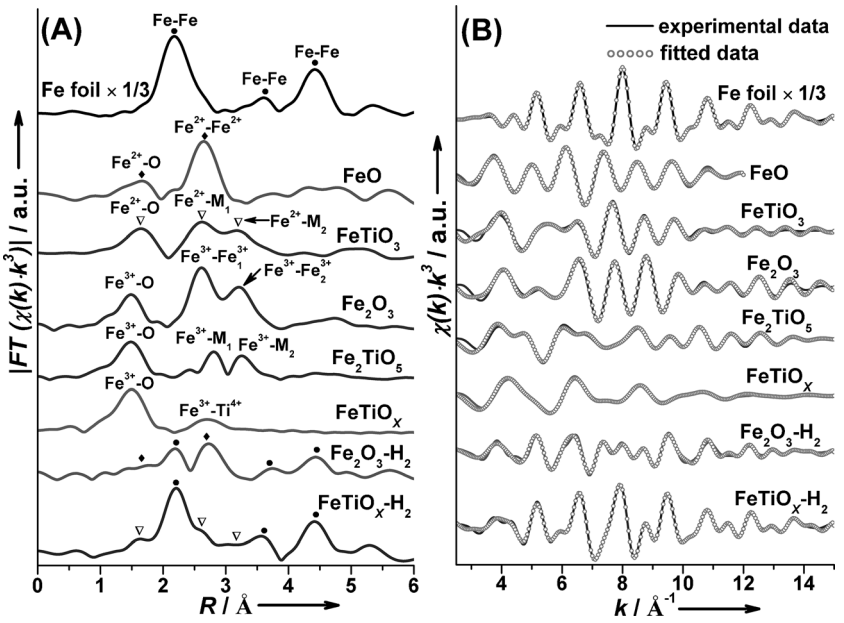

Figure 6. A) Fourier transforms of filtered EXAFS oscillations $k^3\chi(k)$ into R space and B) corresponding filtered $k^3\chi(k)$ of Fe K edge in Fe-containing samples in the k range of 2.5–15 Å^{-1}. The dotted lines correspond to the curve-fitting results in k space calculated by using the FEFF 8.4 code. ● Indicate Fe^0; ◆ FeO; ▽ $FeTiO_3$.

EXAFS oscillations $k^3\chi(k)$ of the Fe K edge in all Fe-containing samples into R space in the k range of 2.5–15 Å^{-1} are shown, and in Figure 6 B, the corresponding filtered $k^3\cdot\chi(k)$ plots are shown, in which the dotted lines correspond to the curve-fitting results in k space calculated by using the FEFF 8.4 code with different reference models. The corresponding curve-fitted data of the Fe K edge are shown in Table 2. The as-prepared $FeTiO_x$ catalyst clearly exhibited a well-defined first Fe–O coordination shell and a rather small second coordination shell, in complete contrast to Fe_2O_3 or Fe_2TiO_5, which exhibit clear bimodal coordination peaks. In our previous study,[34] this unique second coordination shell was attributed to the scattering pathway of Fe–O–Ti, and the Fe–O–Ti bond length was calculated to be 3.09 Å. This bond length was shorter than that in well-crystallized Fe_2TiO_5 (3.18 Å) and belonged to the edge-shared Fe^{3+}–$(O)_2$–Ti^{4+} structure, causing the electronic inductive effect between Fe^{3+} and Ti^{4+} species to take place more easily, thus resulting in its specific deoxidation behavior and high NH_3-SCR performance. The small coordination number of Fe–O–Ti (2.6) in the $FeTiO_x$ catalyst is in good accordance with the XANES results, confirming again the existence of abundant structural defects in iron titanate crystallites, which is advantageous to the adsorption and activation of reactants for the $deNO_x$ process. After H_2 reduction, both the Fe_2O_3 sample and $FeTiO_x$ catalyst presented coordination shells with a mixed state, for which the common peaks in Figure 6 A (indicated by ●) can be attributed to metallic Fe^0 as mentioned above. For H_2-reduced Fe_2O_3, the Fe–O and Fe–O–Fe shells belonging to FeO can be clearly observed (indicated by ◆). As for the H_2-reduced $FeTiO_x$ catalyst, the Fe–O and Fe–O–M (M = Fe or Ti) shells ascribed to $FeTiO_3$ can be observed (indicated by ▽), confirming again that the iron titanate crystallites can be uniformly reduced to ilmenite $FeTiO_3$ phase as a result of the homogeneous Fe^{3+}–$(O)_2$–Ti^{4+} structure with unique deoxidation behavior. These conclusions are well supported by the curve-fitting results of Fe K edge EXAFS (Table 2) with high degree of fit between the experimental data and FEFF-calculated data (Figure 6 B). The relatively small coordination numbers of Fe–Fe shells in the H_2-reduced $FeTiO_x$ catalyst also suggest that the metallic Fe^0 formed after high-temperature reduction exhibited rather small particle sizes, probably resulting from the weak interaction between Fe^0 and the oxide support and also the hindering of Fe^0 aggregation by the in situ released TiO_2.

In a similar way, the Ti K edge EXAFS data of $FeTiO_x$ catalysts before and after H_2 reduction were curve-fitted by the least-square method using different Ti-containing reference models, with the Fourier transformed $k^3\chi(k)$ shown in Figure 7 A in the k range of 2.5–13 Å^{-1} and the filtered $k^3\chi(k)$ shown in Figure 7 B, in which the dotted lines correspond to the FEFF-calculated scattering pathways. The relevant curve-fitted data of Ti K edge EXAFS results are shown in Table 3. Similar to the case of Fe K edge EXAFS experiments, a well-defined first Ti–O coordination shell and a rather small second coordination shell can be observed for the $FeTiO_x$ catalyst, the second shell of which is different from those in anatase TiO_2, rutile TiO_2, or Fe_2TiO_5, which reveal clear bimodal coordination peaks. According to the curve-fitting results, the small second coordination shell of the $FeTiO_x$ catalyst can be attributed to the scattering pathway of Ti–O–Fe with smaller bond length (3.08 Å) than that in Fe_2TiO_5 (3.17 Å). From the perspective of the central Ti species, this bond length can be ascribed to the edge-shared Ti^{4+}–$(O)_2$–Fe^{3+} structure, in which the Ti–O–Fe coordination number is only 2.0 because of the crystallite phase of the $FeTiO_x$ catalyst. After H_2 reduction, not only the first but also the second coordination shells of Ti species revealed some notable variations, exhibiting overlapping peak shapes. Using ilmenite $FeTiO_3$ and rutile TiO_2 as references, the Ti K EXAFS data in the H_2-reduced $FeTiO_x$ catalyst could be well simulated with high fitting degree, which is quite consistent with the Ti K edge XANES results.

Proposed deoxidation process of the $FeTiO_x$ catalyst

Based on the above-mentioned H_2-TPR, XANES linear fitting, and EXAFS curve-fitting results, the specific deoxidation behavior of $FeTiO_x$ catalyst can be proposed as shown in Scheme 1.

Table 2. Calibrated EXAFS curve-fitting results of Fe K edge in different samples (M = Fe or Ti).

Sample	Ref.[a]	Shell	CN[b]	R[c] [Å]	ΔE [eV]	DW[d] [Å]	R factor [%]
Fe foil	Fe	Fe–Fe	8.0 ± 3.7	2.48 ± 0.03	−4.7 ± 7.4	0.072 ± 0.033	0.5
		Fe–Fe_1	6.0 ± 6.8	2.87 ± 0.07	−7.1 ± 12.7	0.081 ± 0.080	
		Fe–Fe_2	12.0 ± 9.6	4.05 ± 0.06	−11.3 ± 6.1	0.099 ± 0.063	
		Fe–Fe_3	24.0 ± 7.7	4.75 ± 0.02	−4.1 ± 2.0	0.092 ± 0.024	
FeO	FeO	Fe–O	6.0 ± 2.3	2.10 ± 0.03	−11.2 ± 4.7	0.092 ± 0.051	1.8
		Fe–O–Fe	12.0 ± 2.6	3.06 ± 0.01	−8.0 ± 1.8	0.108 ± 0.018	
$FeTiO_3$	$FeTiO_3$	Fe–O	6.0 ± 1.2	2.10 ± 0.03	−7.9 ± 3.5	0.097 ± 0.030	6.1
		Fe–O–M_1	4.0 ± 1.0	2.98 ± 0.02	2.1 ± 2.3	0.111 ± 0.022	
		Fe–O–M_2	3.0 ± 1.0	3.38 ± 0.02	17.5 ± 2.5	0.074 ± 0.030	
Fe_2O_3	Fe_2O_3	Fe–O	6.0 ± 1.5	1.95 ± 0.03	−15.1 ± 5.4	0.101 ± 0.037	4.2
		Fe–O–Fe_1	3.0 ± 0.6	2.97 ± 0.02	−2.8 ± 2.3	0.095 ± 0.017	
		Fe–O–Fe_2	3.0 ± 1.0	3.36 ± 0.02	14.0 ± 3.2	0.064 ± 0.028	
Fe_2TiO_5	Fe_2TiO_5	Fe–O	3.0 ± 1.1	1.95 ± 0.02	−15.9 ± 3.3	0.089 ± 0.018	9.0
		Fe–O–M_1	3.0 ± 2.3	3.18 ± 0.04	1.9 ± 7.1	0.072 ± 0.043	
		Fe–O–M_2	3.0 ± 2.7	3.67 ± 0.05	−16.2 ± 7.1	0.093 ± 0.051	
$FeTiO_x$	Fe_2TiO_5	Fe–O	7.7 ± 1.7	1.96 ± 0.01	−8.6 ± 2.2	0.095 ± 0.016	4.5
		Fe–O–Ti	2.6 ± 2.5	3.09 ± 0.04	4.6 ± 4.4	0.104 ± 0.045	
Fe_2O_3-H_2	FeO	Fe–O	4.2 ± 2.9	2.10 ± 0.03	−5.2 ± 3.8	0.099 ± 0.071	7.1
		Fe–O–Fe	8.2 ± 1.8	3.06 ± 0.01	−4.0 ± 1.2	0.107 ± 0.01	
	*Fe	*Fe–Fe	0.8 ± 0.4	2.48 ± 0.03	−2.5 ± 0.6	0.063 ± 0.029	
		*Fe–Fe_1	0.5 ± 0.8	2.87 ± 0.07	−6.8 ± 12.2	0.067 ± 0.066	
		*Fe–Fe_2	1.0 ± 1.6	4.05 ± 0.06	−7.9 ± 0.0	0.072 ± 0.046	
		*Fe–Fe_3	2.2 ± 0.7	4.75 ± 0.02	−4.2 ± 11.3	0.075 ± 0.020	
$FeTiO_x$-H_2	$FeTiO_3$	Fe–O	3.4 ± 2.5	2.10 ± 0.03	−4.4 ± 4.7	0.080 ± 0.081	1.2
		Fe–O–M_1	2.3 ± 0.6	2.98 ± 0.02	1.8 ± 2.8	0.105 ± 0.021	
		Fe–O–M_2	1.7 ± 2.9	3.38 ± 0.02	16.0 ± 0.0	0.070 ± 0.028	
	*Fe	*Fe–Fe	1.5 ± 3.5	2.48 ± 0.03	−4.2 ± 0.1	0.058 ± 0.027	
		*Fe–Fe_1	0.9 ± 2.2	2.87 ± 0.07	−12.6 ± 0.7	0.062 ± 0.061	
		*Fe–Fe_2	2.3 ± 1.9	4.05 ± 0.06	−13.2 ± 1.1	0.077 ± 0.049	
		*Fe–Fe_3	4.7 ± 2.9	4.75 ± 0.02	−3.7 ± 0.1	0.080 ± 0.021	

[a] For information on the calibration of (reference) coordination numbers and the treatment of error margins, see the Experimental Section. [b] Coordination number. [c] Bond length. [d] Debye–Waller factor.

Owing to the homogeneous state of Fe^{3+} species and Ti^{4+} species with electronic inductive effect in the edge-shared Fe^{3+}–$(O)_2$–Ti^{4+} structure of iron titanate crystallites, the Fe^{3+} species with higher oxidation ability can be totally converted into Fe^{2+} species below 500 °C, which is a much easier process than the corresponding reduction of Fe^{3+} species in pristine Fe_2O_3. It is noteworthy that the NH_3-SCR reaction mainly occurs over the $FeTiO_x$ catalyst below 500 °C with high deNO_x efficiency, which is closely related to the enhanced redox ability of Fe^{3+} species in the specific Fe^{3+}–$(O)_2$–Ti^{4+} structure. The as-formed Fe^{2+} species in the H_2-reduced sample combines with Ti^{4+} species to exist as ilmenite $FeTiO_3$, but not as FeO as in the Fe_2O_3 case, indicating again that the Fe species and Ti species are present in a high dispersion state at the atomic scale. Above 500 °C, the surface layers of as-formed $FeTiO_3$ can be further reduced, which results in the formation of partial metallic Fe^0 clusters or particles and residual rutile TiO_2. However, the reduction of Fe^{2+} species in bulk $FeTiO_3$ phase cannot be achieved even at temperatures as high as 900 °C. In short summary, the unique microstructure of iron titanate crystallites in the $FeTiO_x$ catalyst results in the specific deoxidation/redox behavior of the Fe species, thus leading to high NH_3-SCR performance at low temperatures.

Conclusions

The advantageous combination of Fe species and Ti species in the $FeTiO_x$ catalyst resulted in its high NO_x reduction efficiency in the NH_3 selective catalytic reduction (NH_3-SCR) of NO_x with a broad operation temperature window and good SO_2 durability. The unique edge-shared Fe^{3+}–$(O)_2$–Ti^{4+} structure in iron titanate crystallites was confirmed to be the true catalytically active site, with an electronic inductive effect between Fe^{3+} species and Ti^{4+} species leading to the enhanced oxidation ability of Fe^{3+} species. In the H_2-TPR process, the Fe^{3+} species in the $FeTiO_x$ catalyst can be totally reduced to Fe^{2+} species below 500 °C in the form of ilmenite $FeTiO_3$, whereas the Fe^{3+} species in Fe_2O_3 can only be reduced to Fe_3O_4. The typical NH_3-SCR reaction mainly occurs below 500 °C, and the enhanced redox ability of Fe^{3+} species in $FeTiO_x$ catalyst is bene-

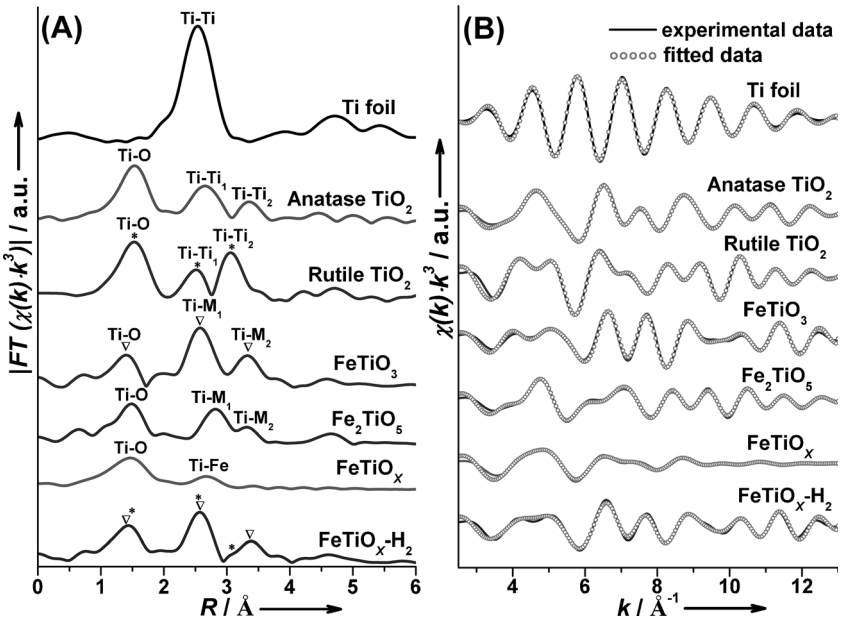

Figure 7. A) Fourier transforms of filtered EXAFS oscillations $k^3\chi(k)$ into R space and B) corresponding filtered $k^3\chi(k)$ of Ti K edge in Ti-containing samples in the k range of 2.5–13 Å^{-1}. The dotted lines correspond to the curve-fitting results in k space calculated by using the FEFF 8.4 code. ● Indicate rutile TiO_2; ▽ $FeTiO_3$.

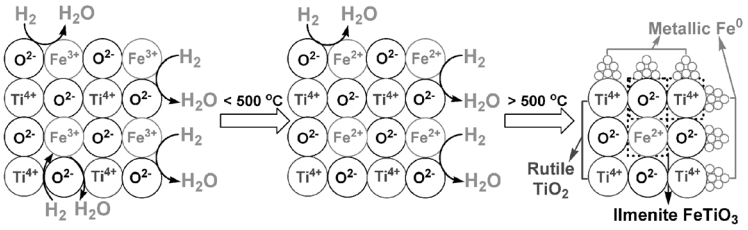

Scheme 1. Proposed H_2 reduction process of the $FeTiO_x$ catalyst.

ficial to enhance its catalytic performance. Based on XANES linear-fitting and EXAFS curve-fitting results, the unique deoxidation behavior of the $FeTiO_x$ catalyst in the H_2-TPR process could be clearly elucidated. The results in this study can supply some ideas for the investigation of the local structure and redox ability of active sites in mixed oxide catalysts simultaneously for certain catalytic reactions.

Experimental Section

Catalyst preparation, NH_3-SCR performance test, and HRTEM characterization

$FeTiO_x$ catalyst with Fe/Ti molar ratio of 1:1 was prepared by a co-precipitation method using $Fe(NO_3)_3{\cdot}9H_2O$ and $Ti(SO_4)_2$ as precursors and $NH_3{\cdot}H_2O$ (25 wt%) as precipitator. The resulting precipitate was filtrated, washed with distilled water, dried at 100 °C for 12 h, and finally calcined in air at 400 °C for 6 h. As reference samples, pristine hematite Fe_2O_3 and anatase TiO_2 were also prepared by the same method. The steady-state NH_3-SCR performance of prepared samples was tested in a fixed-bed quartz tube reactor at atmospheric pressure, and the reaction conditions of standard SCR were controlled as follows: [NO] = [NH_3] = 500 ppm, [O_2] = 5 vol%, and N_2 balance; 0.6 mL catalyst, 20–40 mesh; total flow rate of 500 mL min^{-1}, and gas hourly space velocity (GHSV) of 50 000 h^{-1}. The effluent gas was continuously analyzed by using an FTIR spectrometer (Nicolet Nexus 670) equipped with a heated, low-volume multiple-path gas cell (2 m). The HRTEM images of the $FeTiO_x$ catalyst, hematite Fe_2O_3, and anatase TiO_2 with high magnification were obtained on a JEOL 2011 TEM (JEOL).

H_2-TPR experiments

Prior to the H_2-TPR procedure, the samples (100 mg) were pretreated in a flow of 20 vol% O_2/He (30 mL min^{-1}) at 300 °C for 0.5 h and cooled down to RT. Then the temperature was raised linearly to 900 °C at a rate of 10 °C min^{-1} in a flow of 5 vol% H_2/Ar (30 mL min^{-1}). The H_2 signal (m/z = 2) was monitored online by using a quadrupole mass spectrometer (HPR20, Hiden Analytical Ltd.) to obtain the H_2-TPR profiles. After the reduction temperature reaching 900 °C, the reduced Fe_2O_3 and $FeTiO_x$ samples were naturally cooled to RT under the H_2 protection, and then put into sealed bags for the following XAFS measurements.

XAFS measurements

The XANES and EXAFS spectra of Fe K and Ti K edges were measured in transmission mode at RT on the BL-7C beam line, Photon Factory, KEK, Japan and BL14W1 beam line, Shanghai Synchrotron Radiation Facility (SSRF). The storage ring was operated at 2.5 GeV with 300 mA as an average storage current for the BL-7C beam line and 3.5 GeV with 200 mA as an average storage current for the BL14W1 beam line. The synchrotron radiation beam line was monochromatized with a Si (111) double crystal monochromator, and mirrors were used to eliminate higher harmonics. The incident and transmitted beam intensities were monitored using ionization chambers filled with pure N_2. XAFS data were analyzed by using the REX2000 program (Rigaku Co.). XANES spectra were normalized with edge height. EXAFS oscillation $\chi(k)$ was extracted by using spline smoothing with a Cook–Sayers criterion[43] and weighted by k^3 in order to compensate for the diminishing amplitude in the high k range because of the decay of the photoelectron wave. Thereafter, the filtered k^3-weighted $\chi(k)$ was Fourier transformed into R space (k range: 2.5–15 Å^{-1} for Fe K EXAFS and 2.5–13 Å^{-1} for Ti K EXAFS) with a Hanning function window. In the curve-fitting step, the possible backscattering amplitude and phase shift were calculated by using the FEFF 8.4 code.[44] For standard reference samples, the coordination numbers (CN), the bond lengths (R), the edge corrections (ΔE) and the Debye–Waller factors were all set to be adjustable. And for the catalysts containing confirmed components by XANES linear fitting results, the bond lengths of specific shells were fixed exactly to the

Table 3. Calibrated EXAFS curve-fitting results of Ti K edge in different samples (M = Fe or Ti)

Sample	Ref.[a]	Shell	CN[b]	R[c] [Å]	ΔE [eV]	DW[d] [Å]	R factor [%]
Ti foil	Ti	Ti-Ti	6.0 ± 0.9	2.90 ± 0.01	4.4 ± 1.3	0.095 ± 0.015	1.2
anatase TiO_2	anatase TiO_2	Ti–O	6.0 ± 1.0	1.98 ± 0.01	12.5 ± 2.0	0.101 ± 0.019	1.7
		Ti–O–Ti_1	3.0 ± 0.9	3.02 ± 0.02	4.4 ± 2.9	0.077 ± 0.027	
		Ti–O–Ti_2	3.0 ± 1.6	4.03 ± 0.03	−7.6 ± 4.1	0.088 ± 0.043	
rutile TiO_2	rutile TiO_2	Ti–O	6.0 ± 1.3	1.98 ± 0.02	−6.4 ± 2.9	0.096 ± 0.024	2.9
		Ti–O–Ti_1	2.0 ± 1.2	2.96 ± 0.04	−17.1 ± 6.5	0.071 ± 0.059	
		Ti–O–Ti_2	4.0 ± 1.4	3.57 ± 0.02	−13.0 ± 3.2	0.066 ± 0.035	
$FeTiO_3$	$FeTiO_3$	Ti–O	6.0 ± 1.6	1.86 ± 0.02	−17.2 ± 4.3	0.082 ± 0.039	3.6
		Ti–O–M_1	4.0 ± 0.8	2.96 ± 0.01	−8.4 ± 2.0	0.060 ± 0.024	
		Ti–O–M_2	3.0 ± 1.3	3.38 ± 0.03	9.9 ± 3.5	0.081 ± 0.037	
Fe_2TiO_5	Fe_2TiO_5	Ti–O	6.0 ± 1.1	1.96 ± 0.02	−8.4 ± 2.7	0.105 ± 0.023	3.3
		Ti–O–M_1	3.0 ± 1.4	3.17 ± 0.03	−8.1 ± 4.5	0.082 ± 0.036	
		Ti–O–M_2	3.0 ± 2.8	3.72 ± 0.05	11.0 ± 7.2	0.071 ± 0.094	
$FeTiO_x$	Fe_2TiO_5	Ti–O	6.9 ± 1.7	1.97 ± 0.02	−5.8 ± 2.5	0.125 ± 0.021	6.9
		Ti–O–Fe	2.0 ± 1.7	3.08 ± 0.04	−2.6 ± 2.3	0.119 ± 0.052	
$FeTiO_x$-H_2	$FeTiO_3$	Ti–O	2.8 ± 1.7	1.86 ± 0.02	−13.0 ± 7.5	0.062 ± 0.065	5.8
		Ti–O–M_1	1.9 ± 0.4	2.96 ± 0.01	−7.6 ± 1.6	0.043 ± 0.022	
		Ti–O–M_2	1.5 ± 1.5	3.38 ± 0.03	0.0 ± 0.0	0.072 ± 0.049	
	*rutile TiO_2	*Ti–O	3.2 ± 0.7	1.98 ± 0.02	−7.5 ± 11.2	0.111 ± 0.036	
		*Ti–O–Ti_1	1.1 ± 0.7	2.96 ± 0.04	−25.6 ± 15.2	0.095 ± 0.023	
		*Ti–O–Ti_2	2.1 ± 0.7	3.57 ± 0.02	19.7 ± 1.0	0.102 ± 0.020	

[a] For information on the calibration of (reference) coordination numbers and the treatment of error margins, see the Experimental Section. [b] Coordination number. [c] Bond length. [d] Debye–Waller factor.

values derived from reference samples, and the rest parameters were set to be adjustable. Thus, we adopted the same error intervals of the fixed bond lengths for the studied catalysts as those in reference samples. During this curve-fitting step, the numbers of free parameters for all samples comply with the Nyquist criterion. After the EXAFS curve fitting of standard reference samples (including Fe foil, FeO, $FeTiO_3$, Fe_2O_3, Fe_2TiO_5, Ti foil, anatase TiO_2, and rutile TiO_2), their coordination numbers and bond lengths were all calibrated to the corresponding values in theoretical crystal structures. Thus, more reasonable fitting data could be obtained that were closer to the real situations. Based on the calibrated fitting data of standard reference samples, both the coordination numbers and bond lengths as well as the corresponding error intervals in the studied catalysts were also calibrated.

Acknowledgements

This work was supported by the National Natural Science Foundation of China (51108446), the Ministry of Science and Technology, China (2012AA062506, 2013AA065301), and the Photon Factory, KEK, Japan (Project No. 2012G537). We sincerely thank Prof. Kiyotaka Asakura from Catalysis Research Center, Hokkaido University, Dr. Yasuhiro Niwa from KEK and Prof. Yuying Huang, Zheng Jiang, Shuo Zhang and other staffs from BL14W1 beam line, SSRF for their generous help in XAFS experiments.

Keywords: iron titanate · nitrogen oxides · selective catalytic reduction · deoxidation behavior · redox ability · X-ray absorption fine-structure

[1] S. Beirle, K. F. Boersma, U. Platt, M. G. Lawrence, T. Wagner, *Science* **2011**, *333*, 1737 – 1739.
[2] R. A. Perry, D. L. Siebers, *Nature* **1986**, *324*, 657 – 658.
[3] G. Busca, L. Lietti, G. Ramis, F. Berti, *Appl. Catal. B* **1998**, *18*, 1 – 36.
[4] H. Bosch, F. Janssen, *Catal. Today* **1988**, *2*, 369 – 379.
[5] N.-Y. Topsøe, *Science* **1994**, *265*, 1217 – 1219.
[6] P. Granger, V. I. Parvulescu, *Chem. Rev.* **2011**, *111*, 3155 – 3207.
[7] D. M. Chapman, *Appl. Catal. A* **2011**, *392*, 143 – 150.
[8] M. Casanova, K. Schermanz, J. Llorca, A. Trovarelli, *Catal. Today* **2012**, *184*, 227 – 236.
[9] D. W. Fickel, E. D'Addio, J. A. Lauterbach, R. F. Lobo, *Appl. Catal. B* **2011**, *102*, 441 – 448.
[10] S. Roy, M. S. Hegde, G. Madras, *Appl. Energy* **2009**, *86*, 2283 – 2297.
[11] M. Iwasaki, K. Yamazaki, K. Banno, H. Shinjoh, *J. Catal.* **2008**, *260*, 205 – 216.
[12] U. Deka, A. Juhin, E. A. Eilertsen, H. Emerich, M. A. Green, S. T. Korhonen, B. M. Weckhuysen, A. M. Beale, *J. Phys. Chem. C* **2012**, *116*, 4809 – 4818.
[13] L. Ren, L. Zhu, C. Yang, Y. Chen, Q. Sun, H. Zhang, C. Li, F. Nawaz, X. Meng, F.-S. Xiao, *Chem. Commun.* **2011**, *47*, 9789 – 9791.
[14] J. H. Kwak, R. G. Tonkyn, D. H. Kim, J. Szanyi, C. H. F. Peden, *J. Catal.* **2010**, *275*, 187 – 190.
[15] C. H. F. Peden, J. H. Kwak, S. D. Burton, R. G. Tonkyn, D. H. Kim, J.-H. Lee, H.-W. Jen, G. Cavataio, Y. Cheng, C. K. Lambert, *Catal. Today* **2012**, *184*, 245 – 251.
[16] M. Høj, M. J. Beier, J.-D. Grunwaldt, S. Dahl, *Appl. Catal. B* **2009**, *93*, 166 – 176.
[17] M. Schwidder, S. Heikens, A. De Toni, S. Geisler, M. Berndt, A. Brückner, W. Grünert, *J. Catal.* **2008**, *259*, 96 – 103.

[18] H. Sjövall, L. Olsson, E. Fridell, R. J. Blint, *Appl. Catal. B* **2006**, *64*, 180–188.
[19] S. Brandenberger, O. Kröcher, A. Tissler, R. Althoff, *Catal. Rev.* **2008**, *50*, 492–531.
[20] J. Hun Kwak, H. Zhu, J. H. Lee, C. H. F. Peden, J. Szanyi, *Chem. Commun.* **2012**, *48*, 4758–4760.
[21] F. Li, Y. Zhang, D. Xiao, D. Wang, X. Pan, X. Yang, *ChemCatChem* **2010**, *2*, 1416–1419.
[22] S. Yang, C. Wang, J. Li, N. Yan, L. Ma, H. Chang, *Appl. Catal. B* **2011**, *110*, 71–80.
[23] S. Roy, B. Viswanath, M. S. Hegde, G. Madras, *J. Phys. Chem. C* **2008**, *112*, 6002–6012.
[24] J. Li, H. Chang, L. Ma, J. Hao, R. T. Yang, *Catal. Today* **2011**, *175*, 147–156.
[25] W. Shan, F. Liu, H. He, X. Shi, C. Zhang, *Chem. Commun.* **2011**, *47*, 8046–8048.
[26] W. Shan, F. Liu, H. He, X. Shi, C. Zhang, *ChemCatChem* **2011**, *3*, 1286–1289.
[27] X. Mou, B. Zhang, Y. Li, L. Yao, X. Wei, D. S. Su, W. Shen, *Angew. Chem.* **2012**, *124*, 3044–3048; *Angew. Chem. Int. Ed.* **2012**, *51*, 2989–2993.
[28] N. Apostolescu, B. Geiger, K. Hizbullah, M. T. Jan, S. Kureti, D. Reichert, F. Schott, W. Weisweiler, *Appl. Catal. B* **2006**, *62*, 104–114.
[29] Z. Huang, X. Gu, W. Wen, P. Hu, M. Makkee, H. Lin, F. Kapteijn, X. Tang, *Angew. Chem.* **2013**, *125*, 688–692; *Angew. Chem. Int. Ed.* **2013**, *52*, 660–664.
[30] F. Liu, H. He, C. Zhang, *Chem. Commun.* **2008**, 2043–2045.
[31] F. Liu, H. He, C. Zhang, Z. Feng, L. Zheng, Y. Xie, T. Hu, *Appl. Catal. B* **2010**, *96*, 408–420.
[32] F. Liu, H. He, *J. Phys. Chem. C* **2010**, *114*, 16929–16936.
[33] F. Liu, H. He, C. Zhang, W. Shan, X. Shi, *Catal. Today* **2011**, *175*, 18–25.
[34] F. Liu, K. Asakura, P. Xie, J. Wang, H. He, *Catal. Today* **2013**, *201*, 131–138.
[35] M. A. Khan, S. I. Woo, O. B. Yang, *Int. J. Hydrogen Energy* **2008**, *33*, 5345–5351.
[36] F. Liu, K. Asakura, H. He, W. Shan, X. Shi, C. Zhang, *Appl. Catal. B* **2011**, *103*, 369–377.
[37] X. She, M. Flytzani-Stephanopoulos, *J. Catal.* **2006**, *237*, 79–93.
[38] P. Li, Y. Xin, Q. Li, Z. Wang, Z. Zhang, L. Zheng, *Environ. Sci. Technol.* **2012**, *46*, 9600–9605.
[39] H.-Y. Lin, Y.-W. Chen, C. Li, *Thermochim. Acta* **2003**, *400*, 61–67.
[40] H.-J. Wan, B.-S. Wu, C.-H. Zhang, H.-W. Xiang, Y.-W. Li, B.-F. Xu, F. Yi, *Catal. Commun.* **2007**, *8*, 1538–1545.
[41] Y. Wu, H. Yu, F. Peng, H. Wang, *Mater. Lett.* **2012**, *67*, 245–247.
[42] W. K. Jozwiak, E. Kaczmarek, T. P. Maniecki, W. Ignaczak, W. Maniukiewicz, *Appl. Catal. A* **2007**, *326*, 17–27.
[43] J. W. Cook, D. E. Sayers, *J. Appl. Phys.* **1981**, *52*, 5024–5031.
[44] A. L. Ankudinov, B. Ravel, J. J. Rehr, S. D. Conradson, *Phys. Rev. B* **1998**, *58*, 7565–7576.

Received: July 13, 2013
Published online on October 2, 2013